Geophysical Journal International

Geophys. J. Int. (2024) **239,** 901–913
Advance Access publication 2024 August 28
GJI Seismology

https://doi.org/10.1093/gji/ggae305

Spurious Rayleigh-wave apparent anisotropy near major structural boundaries: a numerical and theoretical investigation

Qicheng Zeng [1], Fan-Chi Lin[1] and Victor C. Tsai [2]

[1] *Department of Geology and Geophysics, University of Utah, Salt Lake City, UT* 84112, *USA. E-mail: Qicheng.Zeng@utah.edu*
[2] *Department of Earth, Environmental and Planetary Sciences, Brown University, Providence, RI* 02912, *USA*

Accepted 2024 August 18. Received 2024 July 19; in original form 2024 March 8

SUMMARY

The recent developments in array-based surface-wave tomography have made it possible to directly measure apparent phase velocities through wave front tracking. While directionally dependent measurements have been used to infer intrinsic 2ψ azimuthal anisotropy (with a 180° periodicity), a few studies have also demonstrated strong but spurious 1ψ azimuthal anisotropy (360° periodicity) near major structure boundaries particularly for long period surface waves. In such observations, Rayleigh waves propagating in the direction perpendicular to the boundary from the slow to the fast side persistently show a higher apparent velocity compared to waves propagating in the opposite direction. In this study, we conduct numerical and theoretical investigations to explore the effect of scattering on the apparent Rayleigh-wave phase velocity measurement. Using 2-D spectral-element numerical wavefield simulations, we first reproduce the observation that waves propagating in opposite directions show different apparent phase velocities when passing through a major velocity contrast. Based on mode coupling theory and the locked mode approximation, we then investigate the effect of the scattered fundamental-mode Rayleigh wave and body waves interfering with the incident Rayleigh wave separately. We show that scattered fundamental-mode Rayleigh waves, while dominating the scattered wavefield, mostly cause short wavelength apparent phase velocity variations that could only be studied if the station spacing is less than about one tenth of the surface wave wavelength. Scattered body waves, on the other hand, cause longer wavelength velocity variations that correspond to the existing real data observations. Because of the sensitivity of the 1ψ apparent anisotropy to velocity contrasts, incorporating such measurements in surface wave tomography could improve the resolution and sharpen the structural boundaries of the inverted model.

Key words: Fourier analysis; Numerical modelling; Seismic anisotropy; Seismic tomography; Surface waves and free oscillations; Wave scattering and diffraction.

1 INTRODUCTION

Seismic anisotropy refers to the phenomenon that seismic waves (e.g. P, S, Rayleigh or Love waves) travel at different speeds depending on the polarization and propagation direction (Long & Becker 2010). Seismic anisotropy potentially provides important information about the deformation history of the Earth (Karato *et al.* 2008). In particular, directionally dependent Rayleigh waves are often used to infer crustal and upper mantle azimuthal anisotropy (Simons *et al.* 2002; Yao *et al.* 2010; Soergel *et al.* 2023). For a laterally homogeneous anisotropic medium (Smith & Dahlen 1973; Montagner & Nataf 1986), Rayleigh-wave azimuthal anisotropy is expected to dominantly vary with a 180° azimuthal periodicity (often referred to as the 2ψ component), where a 360° periodicity (1ψ) is not possible due to the reciprocity principle. This assumption has often been embedded in standard tomographic inversion methods (e.g. Barmin *et al.* 2001).

Despite the theoretical expectation, spurious 1ψ apparent anisotropy has been clearly observed from long-period surface wave studies using earthquakes through wave front tracking particularly near major structural boundaries (Lin & Ritzwoller 2011a; Mauerberger *et al.* 2021). Lin & Ritzwoller (2011a) proposed that the 1ψ anisotropy is related to the finite frequency effect, where unaccounted backward scattered waves from a sharp velocity contrast could bias apparent velocity measurements. While 1ψ anisotropy has also been observed at short periods using ambient noise cross-correlations, the cause has been partially attributed to poor source and station coverage (Mordret *et al.* 2013; Kästle *et al.* 2022). When left unaccounted for, the spurious 1ψ component could bias the targeted intrinsic 2ψ anisotropy observation (Lin & Ritzwoller 2011a;b; Zhang *et al.* 2021; Liu *et al.* 2022).

The objective of this study is to understand the precise physical cause of 1ψ anisotropy. We first extend the study of Lin & Ritzwoller (2011a) to cover the entire contiguous United States and show that

persistent Rayleigh-wave 1ψ anisotropy can be observed across all major velocity structural boundaries. We then simplify our analysis to a 2-D wave propagation problem using velocity contrasts across the northwestern side of Snake River Plain as an example case. 2-D numerical simulations were performed to demonstrate that Rayleigh waves propagating in the opposite direction across a sharp velocity contrast indeed have different apparent phase velocities and hence the spurious 1ψ anisotropy. We test how the 1ψ anisotropy is sensitive to the station spacing and the measuring scheme. We then use mode summation and the locked mode approximation (Harvey 1981) to decompose the 2-D wavefield into fundamental-mode Rayleigh waves and higher modes/body waves. Through the analysis, we conclude that the 1ψ anisotropy is mainly caused by the interference of scattered body waves with the incident/transmitted Rayleigh wave, instead of being caused by the backward scattered Rayleigh wave.

2 USARRAY TRANSPORTABLE ARRAY OBSERVATIONS

Here we briefly summarize the process of making 1ψ measurements across USArray. Over 1400 earthquakes occurred between January 2007 and May 2015 with M_s magnitudes larger than 5.0 are used for Rayleigh-wave dispersion measurements. For each earthquake, we apply automated frequency-time analysis (FTAN; Levshin & Ritzwoller 2001; Lin *et al.* 2008) to measure phase traveltimes at each period for all available stations, which are spaced approximately 70 km apart. The station-wise phase traveltimes are then interpolated onto a $0.2^\circ \times 0.2^\circ$ grid by minimum curvature surface fitting (Smith & Wessel 1990) to construct phase traveltime maps. The spatial gradient of the phase traveltime map is then calculated to approximate local phase slowness and direction of geometric propagation using the eikonal equation (Lin *et al.* 2009).

For each location, using all available phase velocity measurements from different earthquakes, we estimate the directionally dependent phase velocity and its uncertainty based on the mean and standard deviation of the mean within each 20° azimuthal bin. A 9-point (3×3 grid with 0.6° separation) averaging scheme is used to reduce small-scale variations, which also lower the effective resolution to ~200 km. We then apply uncertainty weighted least-square fits to the azimuthally binned phase velocity measurements, using sinusoidal functions (Smith & Dahlen 1973):

$$c(\psi) = c_{\rm iso}\left\{1 + \frac{A_1}{2}\cos(\psi - \varphi_1) + \frac{A_2}{2}\cos[2(\psi - \varphi_2)]\right\}, \quad (1)$$

where $c_{\rm iso}$ is the isotropic phase velocity, ψ is the azimuthal angle measured positive clockwise from north, A_1 and φ_1 are peak-to-peak relative amplitude and fast direction of the 1ψ component and A_2 and φ_2 are peak-to-peak relative amplitude and fast direction of the 2ψ component.

Fig. 1 summarizes the 60-s Rayleigh-wave isotropic phase velocity and 1ψ anisotropy observed across the contiguous United States. The observed 1ψ amplitude is strongest near major structural boundaries and 1ψ fast directions generally point toward the fastest ascent direction of the isotropic phase velocity. For example (Fig. 1, insert), on the northwestern edge of the Snake River Plain, phase velocity measurements with waves propagating to the northwest (toward the fast anomaly) are systematically about 3 per cent faster than measurements with waves propagating to the southeast (toward the slow anomaly). In the Western United States, strong 1ψ anisotropy mainly appears near the physiographic boundaries of Snake River Plain, Green River Basin, Rocky Mountains, Colorado Plateau, Sierra Nevada, Cascade Range and Pasco Basin (Shen & Ritzwoller 2016). To the east, there is also 1ψ anisotropy observed near the edge of the Edwards Plateau, Mississippi Embayment, Virginia Anomaly (Pollitz & Mooney 2016) and Northern Appalachian Anomaly (Menke *et al.* 2016). We note that Lin & Ritzwoller (2011b) have shown that while the observed 1ψ anisotropy amplitudes could be somewhat reduced by incorporating amplitude measurements and solving the full 2-D Helmholtz wave equation when making the phase velocity measurement, the 1ψ anisotropy cannot be eliminated by this process.

3 NUMERICAL SIMULATION

To understand the cause of the 1ψ anisotropy, we synthesize 2-D (x: horizontal and z: vertical) wavefields using the spectral element method (SPECFEM2D; Komatitsch *et al.* 2001) and investigate how apparent Rayleigh-wave phase velocities depend on the direction of wave propagation. We construct our 2-D model with a sharp velocity contrast (Figs 2a-b) using 1-D *Vs* models extracted from Schmandt *et al.* (2015) at two locations near the northwestern Snake River Plain (SRP; Fig. 1). The northwestern SRP is chosen because strong 1ψ anisotropy has been persistently observed there (Fig. 1; Lin & Ritzwoller 2011a). On the left (0–3000 km in x), our model represents velocity structure within the SRP, which is generally slower in the uppermost mantle deeper than 40 km as part of the Yellowstone hotspot track. On the right (3000–6000 km in x), the model represents velocity structure outside of the SRP associated with the Idaho Batholith/Northern Rockies, which is generally faster in the upper mantle. The extracted models are averaged every 10 km depth interval down to 200 km and the velocity at 200 km is extended down to 600 km to avoid boundary distortion. We use empirical relationships of Brocher (2005) to obtain *Vp* and density models from the *Vs* model.

To simulate the 1ψ anisotropy measurement, we perform two numerical simulations with one source on the left and one source on the right. The sources are located at 1 km depth to generate strong Rayleigh waves and 2000 km away from the structural boundary (i.e. at $x = 3000$ km) in horizontal distance, which is sufficient to separate the incident Rayleigh and body waves. Isotropic moment tensor sources are used for the simulation (Feng & Ritzwoller 2017). A dominant source frequency of 0.02 Hz is applied to excite intermediate to long-period Rayleigh waves, for which 1ψ anisotropy has been observed using tectonic scale seismic arrays (Lin & Ritzwoller 2011a; Mauerberger *et al.* 2021). Perfectly matched layer (PML) boundary conditions (Komatitsch & Tromp 2003) are implemented to absorb energy at the boundary and avoid artificial reflections. An example snapshot of the vertical-component wavefield excited by the left source at 740 s lag time is shown in Fig. 2(c), where the transmitted Rayleigh wave, reflected Rayleigh wave, and scattered body wave can be observed. Throughout the numerical simulations, we record waveforms at the surface between 2000 and 4000 km horizontal distance at 1 km intervals (dense blue triangles in Fig. 2b). An example subsampled record section of the vertical waveforms from the left source is shown in Fig. 3. Distinguishable wave types include (i) Incident and transmitted Rayleigh waves (mainly flat-topped due to the plotting amplitude range; (ii) earlier direct P-SV body wave arrivals and (iii) reflected Rayleigh waves from the velocity contrast at $x = 3000$ km. The scattered Rayleigh and body waves cannot be distinguished from the incident Rayleigh wave near the structural boundary due to the finite-frequency nature of the wave train.

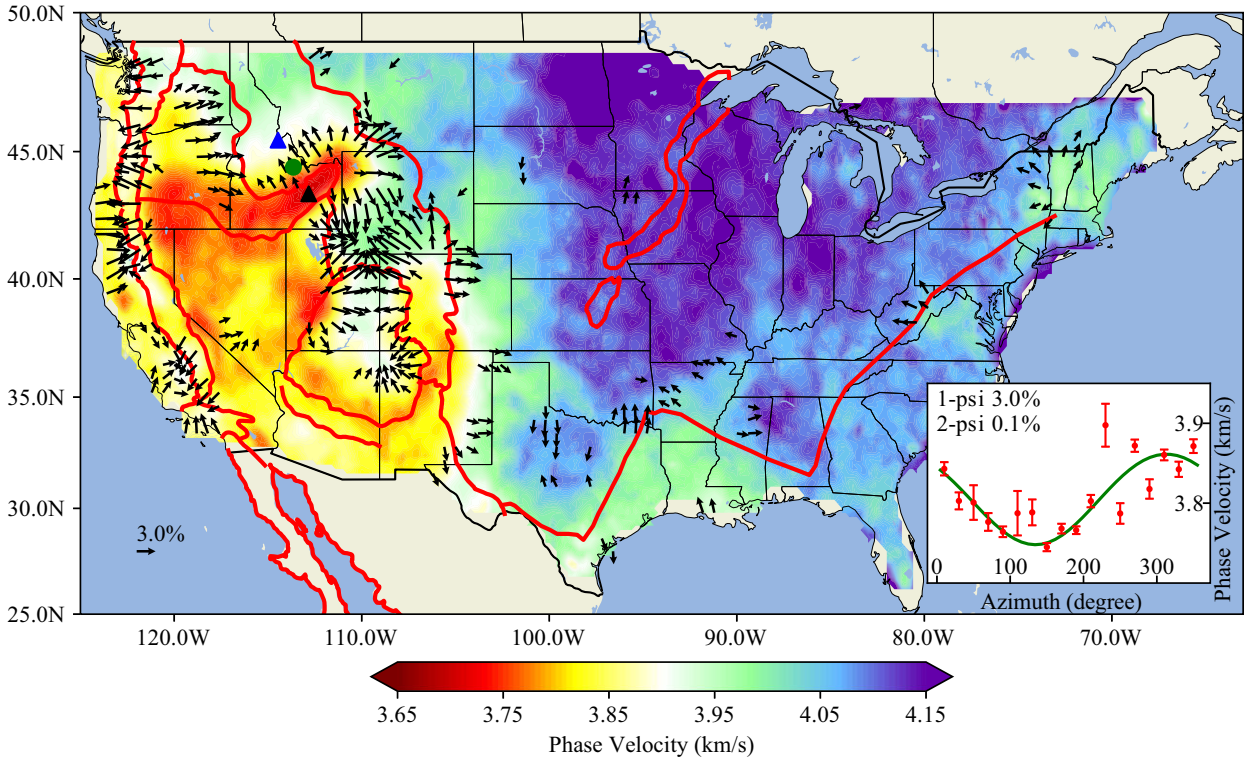

Figure 1. Black arrows show fast directions of 1ψ anisotropy for 60-s Rayleigh waves measured across the contiguous United States using USArray data. Only locations with 1ψ amplitudes larger than 2 per cent are shown where the lengths of the arrows are proportional to the 1ψ amplitude. Isotropic 60-s Rayleigh-wave phase velocities are shown in the background. Major physiographic boundaries are shown with red lines. Blue and black triangles in Idaho near the Snake River Plain denote the two locations where we extract 1-D velocity models for numerical simulations. Inset plot shows the example azimuthally dependent phase-velocity measurements (red error bars) for a point in Idaho denoted by the green circle. The green line shows the best-fitting curve based on eq. (1) where the 1ψ and 2ψ amplitudes are identified in the upper left-hand corner.

To obtain apparent phase velocities, we first apply frequency–time analysis (FTAN; Levshin & Ritzwoller 2001; Lin *et al.* 2008) to measure phase traveltime across the synthetic vertical waveforms observed at the virtual receiver stations. For each adjacent station pair, we then take the spatial derivative of the traveltime to derive the phase slowness (the inverse of phase velocity, Lin *et al.* 2009). For each location, we compare the apparent phase velocities $c_L(x)$ and $c_R(x)$ derived from the left and right sources, respectively, and determine the peak-to-peak 1ψ amplitudes A_1,

$$A_1(x) = \frac{c_L(x) - c_R(x)}{(c_L(x) + c_R(x))/2}. \quad (2)$$

Figs 4(a) and (b) show the phase velocity measurements at 60 s for the left and right sources using 10-km and 70-km station spacing, where the velocities are simply calculated as the ratio of the station spacing to the time difference. For the 70-km result, the velocities of the nearest three stations are averaged, to be consistent with the effective resolution (~200 km) and the process of deriving the 1ψ measurements across USArray (Fig. 1). For the 10-km station spacing result, instead of a constant phase velocity on each side of the vertical boundary as would be predicted by a homogeneous 1-D velocity model, the apparent phase velocity measurements oscillate, especially on the reflected side, near the structure boundary. This indicates scattered surface and body waves are interfering with the incident and transmitted Rayleigh wave. Compared to the 10-km result, short wavelength oscillations near boundary are absent for the 70-km result. The 70-km result also shows that the recovered velocity structure is generally shifted towards the source side relative to the input structure. This is consistent with observations from real data and predictions made based on the finite-frequency sensitivity kernels considering backscattering (Lin & Ritzwoller 2011a). As a result, the 1ψ amplitude A_1 (eq. 2) oscillates near the structural boundary for the 10-km case but gently peaks at the structural boundary for the 70-km case (Fig. 4c).

The different results for different station spacings indicate the apparent 1ψ anisotropy is a localized wave phenomenon which can be overlooked if the station spacing is much longer than the characteristic wavelength. We note that experiments with different source distances, ranging from 1500 to 2500 km away from the structural boundary, do not affect the results presented in Fig. 4. We focus on the 70-km result hereafter to be consistent with USArray station spacing and hence have better comparisons with empirical observations. The positive 1ψ amplitude near the structure boundary represents the fast direction pointing toward the faster structure consistent with the observations (Fig. 1). The simulated 2 per cent 1ψ amplitude is slightly smaller than the observed 3 per cent near the northwestern SRP from real data (Fig. 1). The discrepancy between simulated and observed 1ψ amplitudes potentially indicates that the reference 3-D tomography model (Schmandt *et al.* 2015) is too smoothed and the velocity contrast between the two 1-D velocity models we extracted is not big enough to reflect the true earth structure. Mauerberger *et al.* (2021) has investigated the effects of *Vs* contrast and boundary sharpness to the 1ψ amplitude, where a stronger *Vs* contrast and a sharper boundary (shorter transition width) result in a higher 1ψ amplitude. Their results also show that

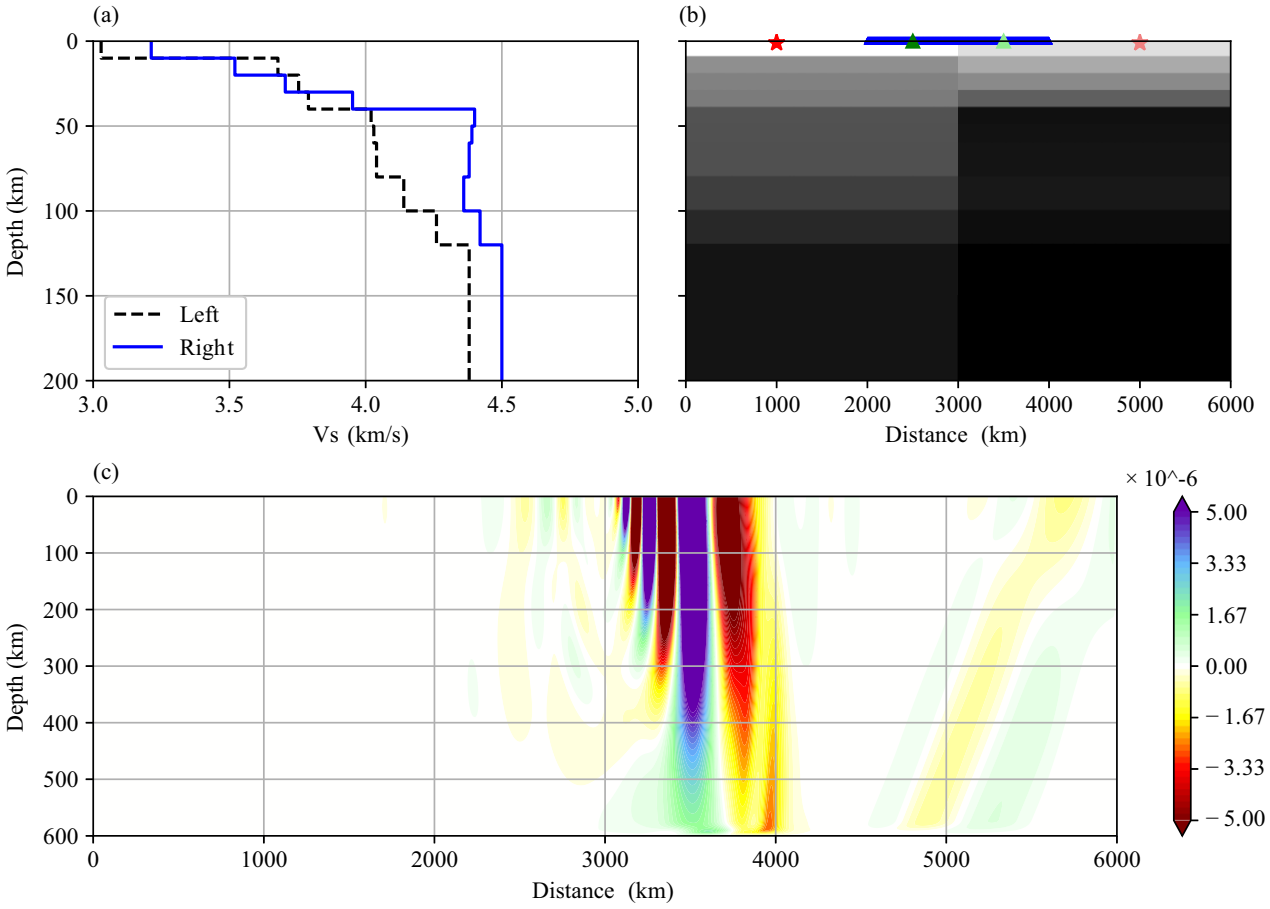

Figure 2. (a) 1-D shear velocity models at two locations near the northwest SRP (Fig. 1) extracted from Schmandt *et al.* (2015). (b) The 2-D *Vs* model used for SPECFEM2D simulations. Background grayscale colors represent shear wave velocities, which can be identified in the 1-D models shown in (a). Red stars represents the left and right sources used in the simulations. The blue line at the surface between 2500 and 3500 km identifies the virtual receiver locations. The green triangles show the virtual stations where template waveforms are used in mode synthetics (Section 4). (c) The vertical component displacement wavefield at 740-s lag time from the SPECFEM2D simulation with the left source.

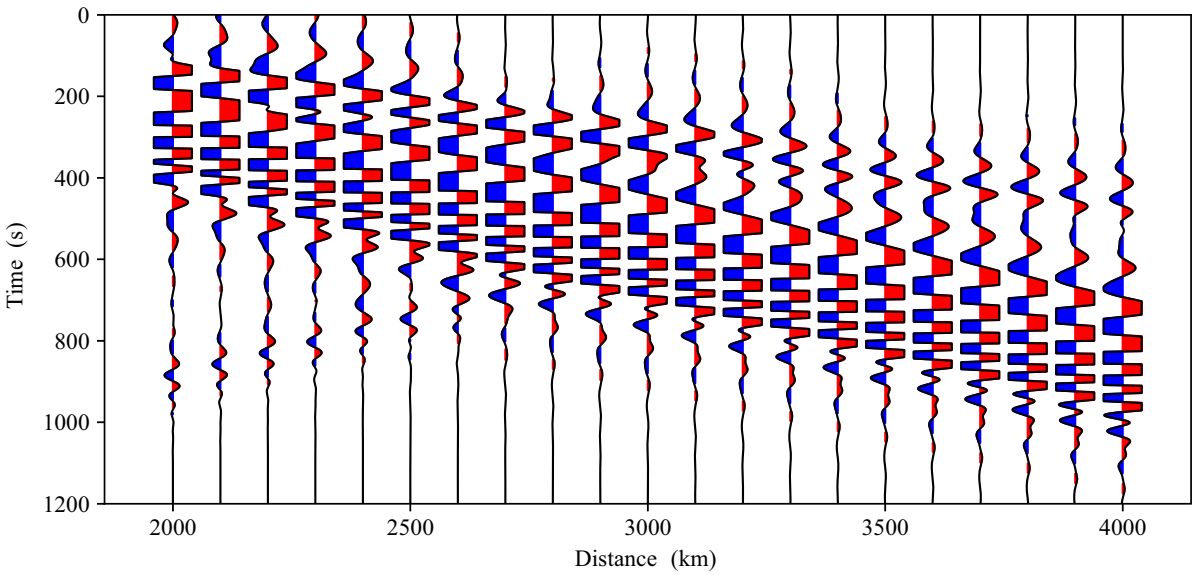

Figure 3. Record section of the vertical-component displacement waveforms filtered between 40 and 100-s period from the SPCEFEM2D simulation using the left source. Red and blue colors represent positive and negative, respectively. Waveforms are flat-topped and normalized by the same threshold value for visualization.

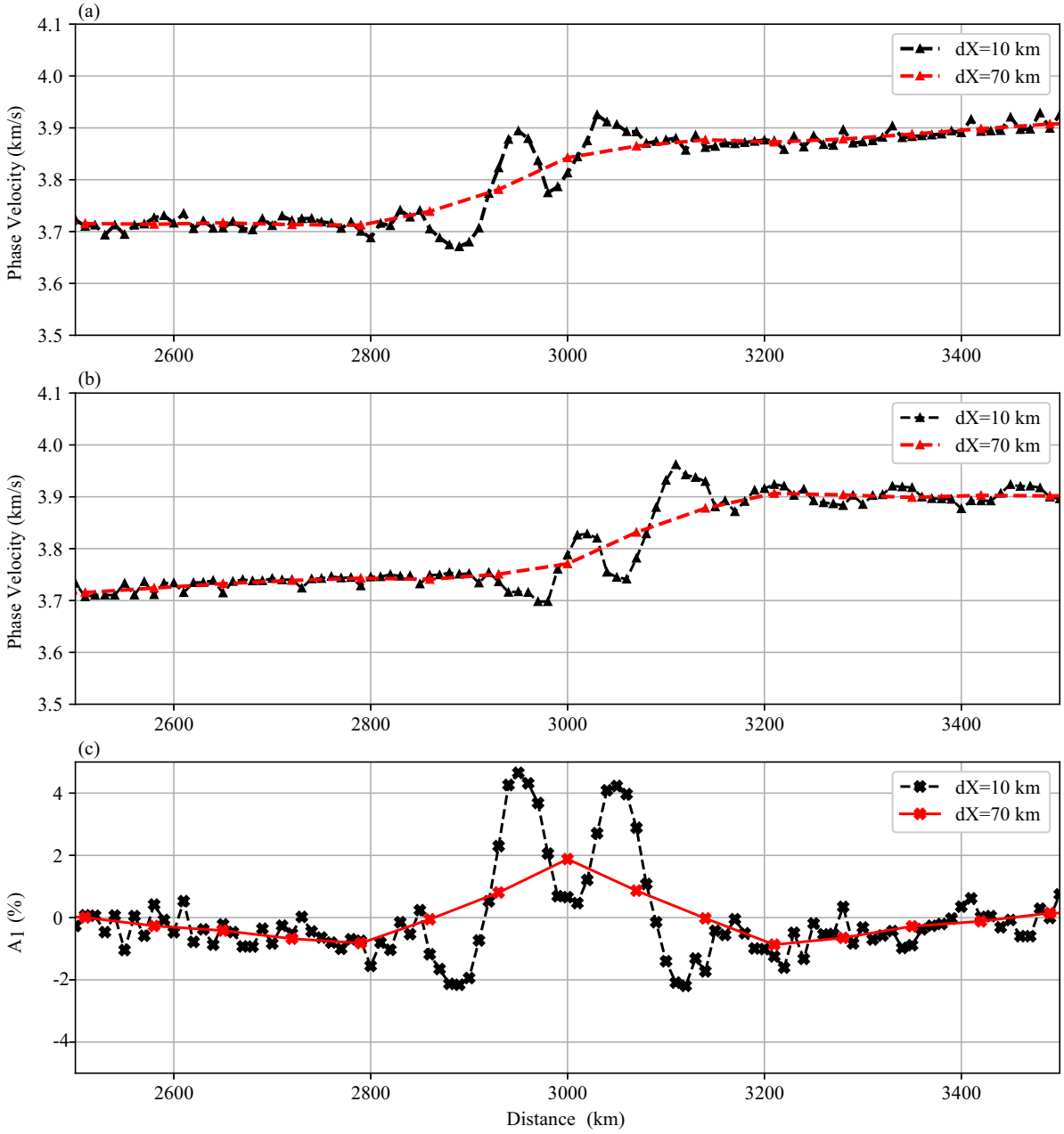

Figure 4. (a) Measured phase velocities at 60 s from the SPECFEM2D synthetics using the left source. Black and red triangles connect by dashed lines represent phase velocity measurements with 10-km and 70-km station spacing (with 3-point smoothing), respectively. (b) Same as (a) but using the right source. (c) 1ψ amplitudes derived from (a) and (b).

1ψ amplitudes become less sensitive to the transition width when the transition width is much smaller than one wavelength. While other factors, such as 3-D lateral scattering, might also contribute to the discrepancy, we believe those effects are secondary and they are outside the scope of this study.

4 NORMAL MODE SUMMATION

Although numerical simulation methods such as finite difference (Li *et al.* 2014), finite element, and spectral element (Komatitsch *et al.* 2001) methods have demonstrated accuracy and efficiency in synthesizing seismic waveforms, it is hard to isolate different components of the wavefield (e.g. surface waves versus body waves). To further understand the nature of the apparent 1ψ anisotropy, we synthesize 2-D waveforms through mode summation and evaluate the effect of scattering surface waves and body waves separately.

4.1 Reflection and transmission coefficients

We adapt the Green's function approach of Its & Yanovskaya (1985) and Datta (2018) to calculate the reflection and transmission coefficients of an incident Rayleigh wave at a vertical boundary. This approach determines reflection and transmission coefficients by satisfying boundary conditions (continuity of displacements and stress), considering orthogonality between modes and assuming weak coupling between surface waves and body waves. A detailed description of this calculation is summarized in Appendix A. We

reformulate the algorithm following the convention from Aki & Richards (2002) and use eigenfunctions from Herrmann (2013) as inputs.

We use the locked mode approximation (Harvey 1981) to artificially include higher modes and use the summation of higher modes to represent body waves based on the mode-ray duality concept (Dahlen & Tromp 1999, pp. 451–513; Zhao & Dahlen 1996). To do this, we modify the model used in the SPECFEM2D simulation (Fig. 2b) by placing an anomalously high-velocity cap layer ($Vs = 6.9$ km s^{-1}) below 900 km depth. The inclusion of this cap layer ensures that body wave energy can be accurately represented by the higher mode summation and that the reflection and transmission coefficient calculation is stable.

Fig. 5 shows the calculated reflection and transmission coefficients for an incident fundamental-mode Rayleigh wave between the two media (Fig. 2a). We calculated the period-dependent coefficients from 10- to 150-s period with 1-s increments. Note that the polarity of the reflection coefficients is reversed for waves propagating from left to right versus right to left due to the impedance contrast. Coefficients associated with the fundamental mode are generally much bigger than the higher modes as the variation between the left and right *Vs* models are mostly smaller than 10 per cent (Fig. 2a).

4.2 Wavefield synthesis from normal mode summation

To construct synthetic wavefields that are comparable to the results from the previous section, we recomposite template waveforms from SPECFEM2D simulations to determine the phase and amplitude content of the incident fundamental-mode Rayleigh waves in our mode summation calculation. Here we take the SPECFEM2D synthetic waveforms 1500 km away from the sources (green triangles in Fig. 2b) as the templates. We taper the template waveforms and remove non-Rayleigh-wave energy slower than 2.5 km s^{-1} and faster than 5 km s^{-1}.

With the vertical displacement spectrum of the fundamental-mode incident wave $F_0(\omega)$ determined at the template location x_0 on the surface, the vertical spectrum of the incident (F_{inc}), reflected (F_{ref}) and transmitted (F_{trans}) waves at other locations (x, z) can be determined based on mode summation:

$$F_{\text{inc}}(x,z,\omega) = r^0(z,\omega)\cdot F_0(\omega)\cdot \exp\left[i\omega\frac{x-x_0}{c_0(\omega)}\right] \tag{3}$$

$$F_{ref}(x,z,\omega) = -\sum_m r^m(z,\omega)\cdot a_m(\omega)\cdot F_0(\omega) \cdot\exp\left[i\omega\left(\frac{x_c-x_0}{c_0(\omega)}+\frac{x_c-x}{c_m(\omega)}\right)\right] \tag{4}$$

$$F_{trans}(x,z,\omega) = \sum_n r^n(z,\omega)\cdot b_n(\omega)\cdot F_0(\omega) \cdot\exp\left[i\omega\left(\frac{x_c-x_0}{c_0(\omega)}+\frac{x-x_c}{c_n(\omega)}\right)\right], \tag{5}$$

where r, a, b and c are vertical displacement eigenfunction, reflection coefficient, transmission coefficient and phase velocity, respectively, with mode index 0 or m for the incident medium or mode index n for the transmitted medium, and ω and x_c representing angular frequency and location of the boundary. Here we follow the Fourier transform convention of Aki & Richards (2002, p. 84). On the incident side, the final synthetic wavefield is the combination of the incident and reflected wavefields:

$$F(x,z,\omega) = F_{\text{inc}}(x,z,\omega) + F_{\text{ref}}(x,z,\omega) \tag{6}$$

Figs 6 and 7 summarize the synthetic wavefield and record sections using the left source and mode summation. When all modes are included (Figs 6a and 7a), the wavefield and record section show incident, transmitted and reflected waves mostly consistent to the SPECFEM2D results shown in Figs 2(c) and 3. The early body-wave arrival is missing in the mode summation calculation due to the tapering of the template waveform. Figs 6(b) and 7(b) show the wavefield and record section when only fundamental-mode Rayleigh waves are included. Overall, Figs 6(a) and (b) and Figs 7(a) and (b) are fairly similar, suggesting that fundamental-mode energy dominates the incident, transmitted and reflection wavefields. Figs 6(c) and 7(c) shows the wavefield and record section when only the higher modes (mode 1–9) are summed together. Stronger forward scattering energy is observed on the transmitted side compared to the backscattering energy. In the context of mode-ray duality, we consider the energy associated with higher modes as body wave energy. This interpretation is consistent with the amplitude decay of the scattered energy away from the structural boundary (Fig. 6c), which suffered from 2-D geometric spreading (Fig. 7c).

We follow the same process as described in Section 3 to measure phase velocity and determine 1ψ anisotropy using synthetic waveforms from modal summation with 70-km station spacing (Fig. 8). The results with and without higher modes are evaluated. When all available modes (mode 0–10) are included, the phase velocities as well as the 1ψ anisotropy overall show consistent results when compared to the SPECFEM2D results (Fig. 4) with minor discrepancies that likely reflect numerical errors in the waveform simulations, reflection/transmission coefficient calculations and the locked mode approximation. The result from fundamental-mode-only synthetics, on the other hand, shows phase velocities and 1ψ anisotropy inconsistent with the SPECFEM2D results, with no obvious 1ψ anisotropy that can be observed.

There are two main differences between the phase velocity measurements including higher mode/body-wave energy or not. First, by including all the higher modes, an apparent shift toward the source side can be observed for the measured phase velocity profile, where the profile is closer to antisymmetric (relative to the boundary) when only the fundamental mode is used. Secondly, on the transmitted side, when higher modes are included, it takes longer before the phase velocity converges to a constant value, reflecting the homogeneous 1-D structure across the boundary. These results suggest that the scattered body-wave energy (mostly forward scattering; Figs 6c and 7c) plays an important role in the observed 1ψ apparent anisotropy.

5 DISCUSSION

In this study, we show that observed spurious Rayleigh-wave apparent 1ψ anisotropy near major structure boundaries is the result of interference between the incident/transmitted Rayleigh waves and scattered waves. Multiple factors are expected to affect the amplitudes and spatial variability of 1ψ anisotropy. First, while not the focus of this study, the sharpness of the boundary and the velocity mismatch across it likely will control the amplitude of the scattered energy (Mauerberger *et al.* 2021). Secondly, the exact interference pattern could be sensitive to the scattered wave type. In our simulation, we show that the interference between the incident and backscattering/reflected Rayleigh waves could dominate and lead to prominent short wavelength oscillations (Fig. 4c) when station spacing is sufficiently dense (relative to the Rayleigh-wave wavelength). For two waves heading in opposite directions with

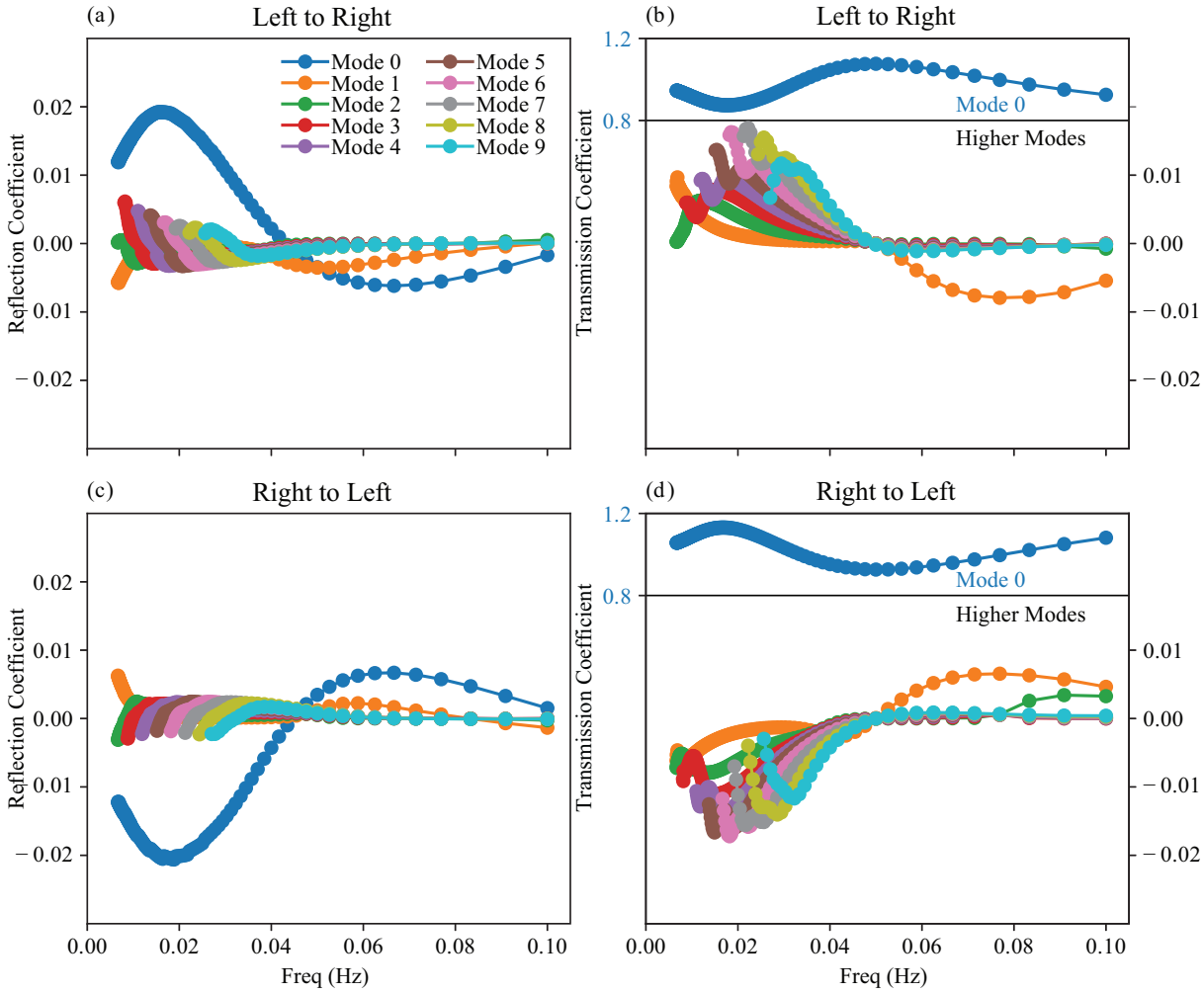

Figure 5. (a) Reflection coefficients for different modes with a fundamental-mode incident Rayleigh wave from the left medium (L) to the right medium (R). (b) Same as (a) but for transmission coefficients. Fundamental mode uses *y*-axis on the left and higher modes use *y*-axis on the right side. (c)–(d) Same as (a)–(b) but from the right medium to the left medium.

the same velocity, the interference pattern is expected to be half of the wavelength. In our example for the 60-s Rayleigh wave with a ∼3.8 km s^{-1} phase velocity, a ∼115 km interference pattern is expected, consistent with observations (Fig. 4c).

The perception that backscattering Rayleigh waves would dominate the scattering wavefield led to the suggestion that this is also the main cause of the observed 1ψ anisotropy in previous studies (Lin & Ritzwoller 2011a). What was not accounted for is that the limited station spacing (relative to the wavelength of the analysed Rayleigh waves) prevented the short wavelength interference pattern from being resolved. Moreover, as shown in our mode summation synthetics, the interference from backscattering Rayleigh waves mostly got canceled out when only low-resolution measurements were being made (Fig. 8c). With 70-km station spacing and 3-point averages, the effective resolution of the measurement is ∼200 km which is comparable to the wavelength of 60-s Rayleigh waves.

To our surprise, scattered body waves, despite being significantly weaker than scattered surface waves, appear to play a much more important role in the low-resolution 1ψ anisotropy measurement. The faster apparent velocity of the scattered body waves could lead to longer apparent wavelengths for the interference pattern (Fig. 8). Because forward scattered body waves are stronger than backscattered body waves, the interference effect on phase velocity measurement is stronger on the transmission side (Figs 8a and b). This is in contrast with the stronger short-wavelength velocity variations on the reflected side for Rayleigh-wave backscattering (Figs 4a and b). This potentially also explains why Helmholtz tomography does not completely remove the spurious 1ψ anisotropy, as it only accounts for interference between Rayleigh waves but not between Rayleigh and body waves (Fig. S1; Lin & Ritzwoller 2011b). Maupin *et al.* (2022) reported 1ψ anisotropy for Love waves, and we suspect a similar interference effect may be responsible.

Given the importance of body wave scattering, any attempts to model the 1ψ anisotropy measurement using simplified 2-D membrane surface-wave finite-frequency sensitivity kernels (e.g. Yang & Forsyth 2006; Tape *et al.* 2007) that only accounts for surface-wave to surface-wave scattering will not be accurate. Full 3-D surface-wave finite-frequency sensitivity kernels (e.g. Zhou *et al.* 2004; Tape *et al.* 2010), on the other hand, do account for surface-wave to body-wave scattering and could be used to model the 1ψ observation and could better resolve the structure boundary. It is interesting to note that Lin & Ritzwoller (2011a) successfully predicted the general 1ψ anisotropy pattern across USArray using a simplified

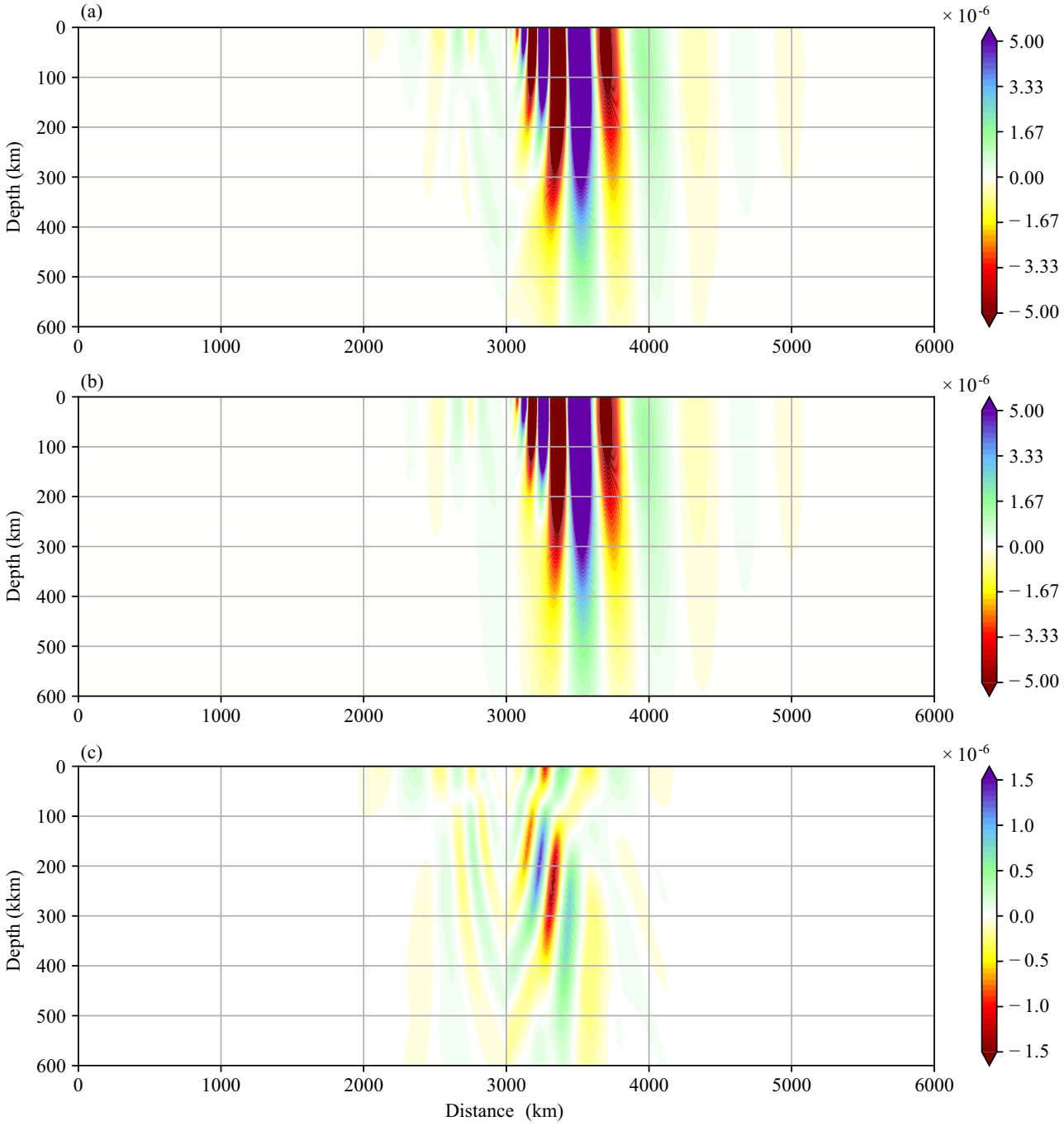

Figure 6. (a) Snapshot of the vertical-component wavefield at 740-s lag time with the left source from normal mode summation using all available modes (mode 0 to 9). (b) Same as (a) but only with the mode 0, that is the fundamental mode. (c) same as (a) but only with the higher modes (mode 1 to 9). Note that the colour bar scales are different for better visualization.

2-D flat-topped surface-wave finite-frequency kernel, suggesting that such kernels do somewhat capture the effect of surface wave to body wave scattering. In principle, when only focusing on the two opposite directions with the largest apparent velocity variation such as the approach taken in this study, the full 3-D kernel can be simplified to a 2-D kernel with one depth dimension and one horizontal dimension.

Two future directions are the natural extensions of this theoretical/numerical focused study. First, a more detailed study could be done across dense seismic arrays to investigate if the short wavelength interference pattern related to surface-wave backscattering could be observed. While dense station coverage in 2-D is rare, dense linear arrays that cut perpendicularly across major physiographic boundaries are not uncommon (e.g. West *et al.* 2004). Moreover, recent dense nodal geophone deployments (e.g. Rabade *et al.* 2023; Wu *et al.* 2023) would also make it possible to investigate detailed interference patterns for short-period surface waves extracted from noise cross-correlations. Recent developments in

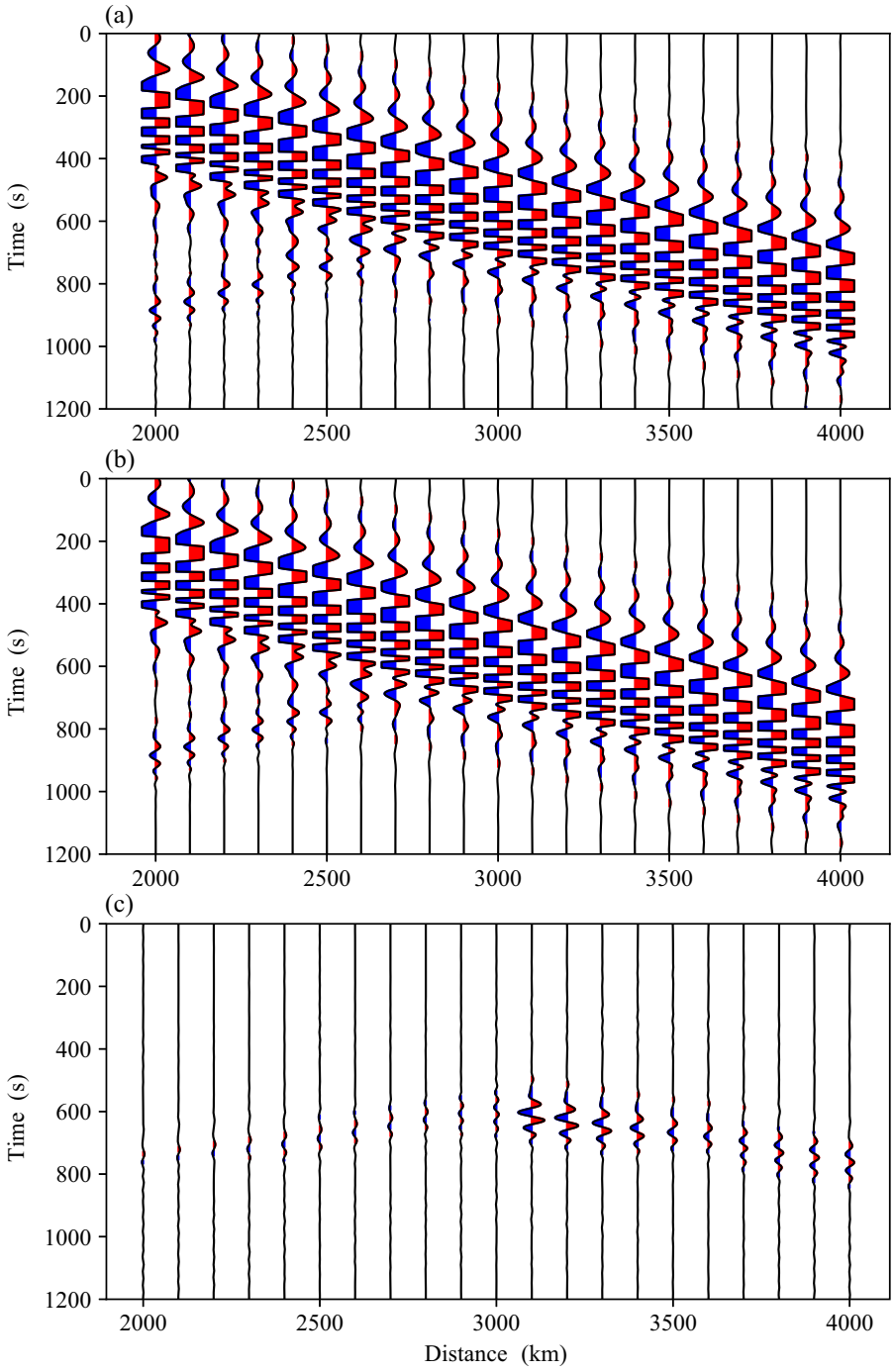

Figure 7. (a) Record section for vertical synthetic waveforms from normal mode summation (all modes included) using the left source. Waveforms are filtered between 40 and 100 s, flat-topped and normalized by the same threshold value for visualization. (b) Same as (a) but with only the fundamental mode included. (c) Same as (a) but only with higher modes (i.e. mode 1–9) included.

array processing have made it possible to conserve the entire wave property of the noise cross-correlation wavefield (Bowden *et al.* 2015), and we expect the exact same interference effect described in this study to be applicable to noise cross-correlation studies, despite the higher frequencies and shorter length scales.

Secondly, better constraints on structure boundaries could be derived from apparent 1ψ anisotropy observations. When unaccounted for, the apparent velocity variations introduced by wave interference discussed in this study not only smooths tomographic images but could also produce systematic biases. This is on top of the fact that the apparent 1ψ anisotropy could bias the intrinsic 2ψ anisotropy observations when azimuthal data coverage is not ideal (Lin & Ritzwoller 2011a; Zhang *et al.* 2021; Liu *et al.* 2022). While it is beyond the scope of this study, we envision that finite-frequency sensitivity kernels regarding 1ψ anisotropy could be constructed through the adjoint method (Tromp *et al.* 2005; Yuan *et al.* 2016; Liu 2020) given an accurate forward calculation algorithm. While the mode summation method works

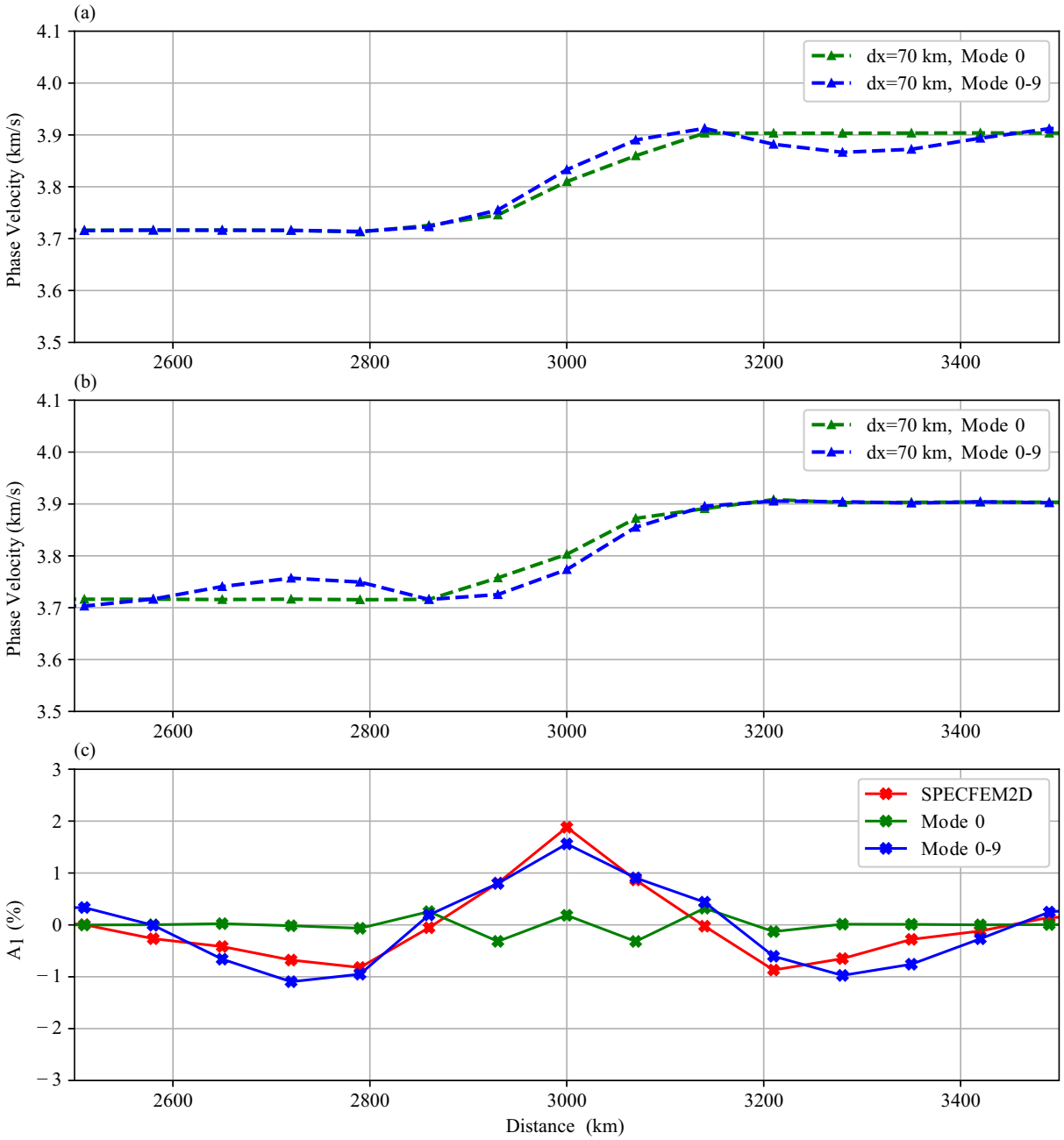

Figure 8. Same as Fig. 4 but from mode summation (green for mode 0 and blue for modes 0–9). Only the results with 70-km station spacing and 3-point averages are shown. The 1ψ amplitude from SPECFEM2D simulation (red) is also shown in (c) for comparison.

well for simple structure boundaries with a homogeneous structure on either side, 2-D or 3-D finite-different/finite-element simulations would offer more flexibility to account for 2-D/3-D velocity structure.

6 CONCLUSIONS

In this study, we use USArray Transportable Array to measure directionally dependent phase velocities across the contiguous United States from teleseismic earthquakes. We show that apparent 1ψ anisotropy (with 360° periodicity) can be observed near major structural contrasts with fast directions that align with the fastest ascent direction of phase velocity structure. To better understand the cause of this spurious and apparent 1ψ anisotropy, we perform 2-D numerical simulations using SPCEFEM2D and show that we can reproduce the 1ψ anisotropy observations when sparse station spacing is used. We also show that a shorter wavelength 1ψ anisotropy variation that has not been observed in real data can also be observed when denser station coverage is available. By separating the incident/transmitted fundamental-mode Rayleigh wave, reflected fundamental-mode Rayleigh wave, and scattered body wave through mode summation, we isolate the effect of interference for scattered Rayleigh waves and body waves. We show that the short and long wavelength 1ψ anisotropy variations are due to the interference of scattered Rayleigh and body waves with the incident/transmitted Rayleigh wave, respectively. As dense array

experiments have become more common in recent year, we envision apparent 1ψ anisotropy could become a standard measurement. And future studies could incorporate such measurements to better resolve structural boundaries in otherwise commonly smoothed tomography models.

ACKNOWLEDGMENTS

This study was supported by National Science Foundation EAR-1753362. We thank Xiongwei Liu, Aurélien Mordret, an anonymous reviewer and the editor Carl Tape for their constructive comments.

AUTHOR CONTRIBUTIONS

Qicheng Zeng (Data curation, Formal analysis, Investigation, Methodology, Software, Validation, Visualization, Writing – original draft, Writing – review & editing); Fan-Chi Lin (Conceptualization, Data curation, Funding acquisition, Methodology, Project administration, Resources, Supervision, Writing – review & editing) and Victor C. Tsai (Methodology, Writing – review & editing).

SUPPORTING INFORMATION

Supplementary data are available at *GJIRAS* online.

Figure S1. Similar to Fig. 4 but applying Helmholtz correction to measure phase velocity and 1ψ amplitudes with 10-km and 70-km station spacing.

Please note: Oxford University Press is not responsible for the content or functionality of any supporting materials supplied by the authors. Any queries (other than missing material) should be directed to the corresponding author for the paper.

CONFLICT OF INTEREST STATEMENT

The authors acknowledge that there are no conflicts of interest recorded.

DATA AVAILABILITY

Phase velocity measurements for contiguous United States, codes for calculation of Rayleigh wave reflection and transmission coefficients, surface wave waveform from propagation and 2-D wavefield from normal mode summation can be found at github (https://github.com/QichengZengSeis/1psi_SurfRT). 2-D wavefield simulation is performed using the SPECFEM2D package (https://github.com/SPECFEM/specfem2d).

REFERENCES

Aki, K. & Richards, P.G., 2002. *Quantitative Seismology,* 2nd edn, Univ. Science Books.

Barmin, M.P., Ritzwoller, M.H. & Levshin, A.L., 2001. A fast and reliable method for surface wave tomography, in *Monitoring the Comprehensive Nuclear-test-ban Treaty: Surface Waves,* pp. 1351–1375, eds, Levshin, A.L. & Ritzwoller, M.H., Birkhäuser Basel.

Bowden, D.C., Tsai, V.C. & Lin, F.-C., 2015. Site amplification, attenuation and scattering from noise correlation amplitudes across a dense array in Long Beach, *Geophys. Res. Lett.,* **42,** 1360–1367.

Brocher, T.M., 2005. Empirical relations between elastic wavespeeds and density in the Earth's crust, *Bull. seism. Soc. Am.,* **95**(6), 2081–2092.

Dahlen, F. & Tromp, J., 1999. *Theoretical Global Seismology,* Princeton Univ. Press.

Datta, A., 2018. SWRT: a package for semi-analytical solutions of surface wave propagation, including mode conversion, across transversely aligned vertical discontinuities, *Geosci. Instrum., Methods Data Syst.,* **7**(1), 101–112.

Denolle, M.A., Dunham, E.M. & Beroza, G.C., 2012. Solving the surface-wave eigenproblem with Chebyshev spectral collocation, *Bull. seism. Soc. Am.,* **102**(3), 1214–1223.

Feng, L. & Ritzwoller, M.H., 2017. The effect of sedimentary basins on surface waves that pass through them, *Geophys. J. Int.,* **211**(1), 572–592.

Harvey, D.J., 1981. Seismogram synthesis using normal mode superposition: the locked mode approximation, *Geophys. J. Int.,* **66**(1), 37–69.

Herrmann, R.B., 2013. Computer programs in seismology: an evolving tool for instruction and research, *Seismol. Res. Lett.,* **84**(6), 1081–1088.

Its, E.N. & Yanovskaya, T.B., 1985. Propagation of surface waves in a half-space with vertical, inclined or curved interfaces, *Wave Motion,* **7**(1), 79–94.

Karato, S.I., Jung, H., Katayama, I. & Skemer, P., 2008. Geodynamic significance of seismic anisotropy of the upper mantle: new insights from laboratory studies, *Annu. Rev. Earth planet. Sci.,* **36,** 59–95.

Kästle, E.D., Molinari, I., Boschi, L. & Kissling, E., & AlpArray Working Group, 2022. Azimuthal anisotropy from eikonal tomography: example from ambient-noise measurements in the AlpArray network, *Geophys. J. Int.,* **229**(1), 151–170.

Komatitsch, D., Martin, R., Tromp, J., Taylor, M.A. & Wingate, B.A., 2001. Wave propagation in 2-D elastic media using a spectral element method with triangles and quadrangles, *J. Comput. Acoust.,* **9**(02), 703–718.

Komatitsch, D. & Tromp, J., 2003. A perfectly matched layer absorbing boundary condition for the second-order seismic wave equation, *Geophys. J. Int.,* **154**(1), 146–153.

Levshin, A.L. & Ritzwoller, M.H., 2001. Automated detection, extraction, and measurement of regional surface waves, in *Monitoring the Comprehensive Nuclear-test-ban Treaty: Surface Waves,* pp. 1531–1545, eds, Levshin, A.L. & Ritzwoller, M.H., Birkhäuser Basel.

Li, D., Helmberger, D., Clayton, R.W. & Sun, D., 2014. Global synthetic seismograms using a 2-D finite-difference method, *Geophys. J. Int.,* **197**(2), 1166–1183.

Lin, F.C., Moschetti, M.P. & Ritzwoller, M.H., 2008. Surface wave tomography of the western United States from ambient seismic noise: rayleigh and Love wave phase velocity maps, *Geophys. J. Int.,* **173**(1), 281–298.

Lin, F.C. & Ritzwoller, M.H., 2011a. Apparent anisotropy in inhomogeneous isotropic media, *Geophys. J. Int.,* **186**(3), 1205–1219.

Lin, F.C. & Ritzwoller, M.H., 2011b. Helmholtz surface wave tomography for isotropic and azimuthally anisotropic structure, *Geophys. J. Int.,* **186**(3), 1104–1120.

Lin, F.C., Ritzwoller, M.H. & Snieder, R., 2009. Eikonal tomography: surface wave tomography by phase front tracking across a regional broadband seismic array, *Geophys. J. Int.,* **177**(3), 1091–1110.

Liu, C., Zhang, S., Sheehan, A.F. & Ritzwoller, M.H., 2022. Surface wave isotropic and azimuthally anisotropic dispersion across Alaska and the Alaska-Aleutian subduction zone, *J. geophys. Res.,* **127**(11), e2022JB024885.

Liu, X., 2020. Finite-frequency sensitivity kernels for seismic noise interferometry based on differential time measurements, *J. geophys. Res.,* **125**(4), e2019JB018932.

Long, M.D. & Becker, T.W., 2010. Mantle dynamics and seismic anisotropy, *Earth planet. Sci. Lett.,* **297**(3-4), 341–354.

Mauerberger, A., Maupin, V., Gudmundsson, Ó. & Tilmann, F., 2021. Anomalous azimuthal variations with 360° periodicity of Rayleigh phase velocities observed in Scandinavia, *Geophys. J. Int.,* **224**(3), 1684–1704.

Maupin, V., Mauerberger, A. & Tilmann, F., 2022. The radial anisotropy of the continental lithosphere from analysis of Love and Rayleigh wave phase velocities in Fennoscandia, *J. geophys. Res.,* **127**(10), e2022JB024445.

Menke, W., Skryzalin, P., Levin, V., Harper, T., Darbyshire, F. & Dong, T., 2016. The Northern Appalachian anomaly: a modern asthenospheric upwelling, *Geophys. Res. Lett.,* **43**(19), 10–173.

Montagner, J.P. & Nataf, H.C., 1986. A simple method for inverting the azimuthal anisotropy of surface waves, *J. geophys. Res.,* **91**(B1), 511–520.

Mordret, A., Shapiro, N.M., Singh, S., Roux, P., Montagner, J.P. & Barkved, O.I., 2013. Azimuthal anisotropy at Valhall: the Helmholtz equation approach, *Geophys. Res. Lett.,* **40**(11), 2636–2641.

Pollitz, F.F. & Mooney, W.D., 2016. Seismic velocity structure of the crust and shallow mantle of the Central and Eastern United States by seismic surface wave imaging, *Geophys. Res. Lett.,* **43**(1), 118–126.

Rabade, S., Lin, F.C., Tape, C., Ward, K.M., Waldien, T. & Allam, A., 2023. The crustal magmatic structure beneath the Denali Volcanic Gap imaged by a dense linear seismic array, *J. geophys. Res.,* **128**(12), e2023JB027152.

Schmandt, B., Lin, F.C. & Karlstrom, K.E., 2015. Distinct crustal isostasy trends east and west of the Rocky Mountain Front, *Geophys. Res. Lett.,* **42**(23), 10–290.

Shen, W. & Ritzwoller, M.H., 2016. Crustal and uppermost mantle structure beneath the United States, *J. geophys. Res.,* **121**(6), 4306–4342.

Simons, F.J., Van Der Hilst, R.D., Montagner, J.P. & Zielhuis, A., 2002. Multimode Rayleigh wave inversion for heterogeneity and azimuthal anisotropy of the Australian upper mantle, *Geophys. J. Int.,* **151**(3), 738–754.

Smith, M.L. & Dahlen, F.A., 1973. The azimuthal dependence of Love and Rayleigh wave propagation in a slightly anisotropic medium, *J. geophys. Res.,* **78**(17), 3321–3333.

Smith, W.H. & Wessel, P., 1990. Gridding with continuous curvature splines in tension, *Geophysics,* **55**(3), 293–305.

Soergel, D., Pedersen, H.A., Bodin, T., Paul, A. & Stehly, L., 2023. Bayesian analysis of azimuthal anisotropy in the Alpine lithosphere from beamforming of ambient noise cross-correlations, *Geophys. J. Int.,* **232**(1), 429–450.

Tape, C., Liu, Q., Maggi, A. & Tromp, J., 2010. Seismic tomography of the southern California crust based on spectral-element and adjoint methods, *Geophys. J. Int.,* **180**(1), 433–462.

Tape, C., Liu, Q. & Tromp, J., 2007. Finite-frequency tomography using adjoint methods—Methodology and examples using membrane surface waves, *Geophys. J. Int.,* **168**(3), 1105–1129.

Tromp, J., Tape, C. & Liu, Q., 2005. Seismic tomography, adjoint methods, time reversal and banana-doughnut kernels, *Geophys. J. Int.,* **160**(1), 195–216.

West, M., Ni, J., Baldridge, W.S., Wilson, D., Aster, R., Gao, W. & Grand, S., 2004. Crust and upper mantle shear wave structure of the southwest United States: implications for rifting and support for high elevation, *J. geophys. Res.,* **109**(B3), doi:10.1029/2003JB002575.

Wu, S.M., Huang, H.H., Lin, F.C., Farrell, J. & Schmandt, B., 2023. Extreme seismic anisotropy indicates shallow accumulation of magmatic sills beneath Yellowstone caldera, *Earth planet. Sci. Lett.,* **616,** 118244.

Yang, Y. & Forsyth, D.W., 2006. Regional tomographic inversion of the amplitude and phase of Rayleigh waves with 2-D sensitivity kernels, *Geophys. J. Int.,* **166**(3), 1148–1160.

Yao, H., van Der Hilst, R.D. & Montagner, J.P., 2010. Heterogeneity and anisotropy of the lithosphere of SE Tibet from surface wave array tomography, *J. geophys. Res.,* **115**(B12), doi:10.1029/2009JB007142.

Yuan, Y.O., Simons, F.J. & Tromp, J., 2016. Double-difference adjoint seismic tomography, *Geophys. J. Int.,* **206**(3), 1599–1618.

Zhang, S., Wang, H., Wu, M. & Ritzwoller, M.H., 2021. Isotropic and azimuthally anisotropic Rayleigh wave dispersion across the Juan de Fuca and Gorda plates and US Cascadia from earthquake data and ambient noise two-and three-station interferometry, *Geophys. J. Int.,* **226**(2), 862–883.

Zhao, L. & Dahlen, F.A., 1996. Mode-sum to ray-sum transformation in a spherical and an aspherical Earth, *Geophys. J. Int.,* **126**(2), 389–412.

Zhou, Y., Dahlen, F.A. & Nolet, G., 2004. Three-dimensional sensitivity kernels for surface wave observables, *Geophys. J. Int.,* **158**(1), 142–168.

APPENDIX A: SURFACE-WAVE REFLECTION AND TRANSMISSION COEFFICIENTS ALGORITHM REFORMULATION

In the case of two layered models with a vertical boundary in the middle, we can estimate reflection and transmission coefficients by satisfying boundary conditions, that is continuity of displacements and stresses at the vertical boundary. For a given angular frequency ω, we assume that the incident wave consists of only one normal mode (sth for generalization of derivation below; $s = 0$ for fundamental mode used in the paper) and that the reflected and transmitted waves contain all possible normal modes within their media. There are possible body waves scattered at the boundary which we also include in the boundary conditions:

$$\boldsymbol{u}_s(z) + \sum_{m=0}^{M} a_m \boldsymbol{u}_m^*(z) + \boldsymbol{u}_b^{(I)}(z) = \sum_{n=0}^{N} b_n \boldsymbol{u}_n(z) + \boldsymbol{u}_b^{(T)}(z) \tag{A1}$$

$$\boldsymbol{\tau}_s(z) + \sum_{m=0}^{M} a_m \boldsymbol{\tau}_m^*(z) + \boldsymbol{\tau}_b^{(I)}(z) = \sum_{n=0}^{N} b_n \boldsymbol{\tau}_n(z) + \boldsymbol{\tau}_b^{(T)}(z) \tag{A2}$$

where $\boldsymbol{u}$ and $\boldsymbol{\tau}$ are displacement and stress vectors. The left-hand side of eq. (A1) corresponds to the incident medium where we have incident sth mode surface wave $\boldsymbol{u}_s$, reflected waves $\sum_{m=0}^{M} a_m \boldsymbol{u}_m^*$, and scattered body wave $\boldsymbol{u}_b^{(I)}$. Reflected waves consist of all possible modes (0 to M) in the first medium, a_m is reflection coefficient, $*$ means complex conjugate due to propagation direction. The right-hand side of eq. (A1) corresponds to the transmitted medium where we have transmitted waves $\sum_{n=0}^{N} b_n \boldsymbol{u}_n$ and scattered body wave $\boldsymbol{u}_b^{(T)}$. Transmitted waves consist of all possible modes (0 to N) in the second medium, b_n is the transmission coefficient. Eq. (A2) is the same boundary condition as eq. (A1) but for stress. Hereafter mode indices s and m always correspond to the incident medium. Mode index n always corresponds to the transmitted medium. In case of any ambiguity, we use superscript (I) and (T) to indicate the medium.

Different normal modes in the same medium are orthogonal, including incident and reflected normal modes:

$$\int_0^\infty \left(\boldsymbol{\tau}_k^* \boldsymbol{u}_m - \boldsymbol{\tau}_m \boldsymbol{u}_k^*\right) \mathrm{d}z = 0, \ km \tag{A3}$$

$$\int_0^\infty \left(\boldsymbol{\tau}_k \boldsymbol{u}_m - \boldsymbol{\tau}_m \boldsymbol{u}_k\right) \mathrm{d}z = 0 \tag{A4}$$

We assume that the body wavefield have weak coupling with reflected and transmitted normal modes (Its & Yanovskaya 1985), that is the wavefields are approximately orthogonal:

$$\int_0^\infty \left[\boldsymbol{\tau}_m \left(\boldsymbol{u}_b^{(2)} - \boldsymbol{u}_b^{(1)}\right) - \boldsymbol{u}_m \left(\boldsymbol{\tau}_b^{(2)} - \boldsymbol{\tau}_b^{(1)}\right)\right] \mathrm{d}z = 0 \tag{A5}$$

$$\int_0^\infty \left[\boldsymbol{\tau}_n^* \left(\boldsymbol{u}_b^{(2)} - \boldsymbol{u}_b^{(1)}\right) - \boldsymbol{u}_n^* \left(\boldsymbol{\tau}_b^{(2)} - \boldsymbol{\tau}_b^{(1)}\right)\right] \mathrm{d}z = 0 \tag{A6}$$

Taking assumptions (A3)–(A6) into account, we solve the boundary conditions by taking the depth integral form (or Green's function approach). Reflection coefficients for the mth mode can then be calculated by $\int_0^\infty [(A1) \cdot \boldsymbol{\tau}_m - (A2) \cdot \boldsymbol{u}_m] \mathrm{d}z$, and

transmission coefficients for the nth mode can be calculated by $\int_0^\infty [(A1)\cdot \boldsymbol{\tau}_n^* - (A2)\cdot \boldsymbol{u}_n^*]\mathrm{d}z$,

$$a_m = \frac{-1}{\int_0^\infty \left(\boldsymbol{\tau}_m^* \boldsymbol{u}_m - \boldsymbol{\tau}_m \boldsymbol{u}_m^*\right)\mathrm{d}z} \sum_{n=0}^{N} b_n \int_0^\infty \left(\boldsymbol{\tau}_m \boldsymbol{u}_n - \boldsymbol{\tau}_n \boldsymbol{u}_m\right)\mathrm{d}z \tag{A7}$$

$$b_n = \frac{1}{\int_0^\infty \left(\boldsymbol{\tau}_n^* \boldsymbol{u}_n - \boldsymbol{\tau}_n \boldsymbol{u}_n^*\right)\mathrm{d}z} \int_0^\infty \left(\boldsymbol{\tau}_n^* \boldsymbol{u}_s - \boldsymbol{\tau}_s \boldsymbol{u}_n^*\right)\mathrm{d}z + \frac{1}{\int_0^\infty \left(\boldsymbol{\tau}_n^* \boldsymbol{u}_n - \boldsymbol{\tau}_n \boldsymbol{u}_n^*\right)\mathrm{d}z} \sum_{m=0}^{M} a_m \int_0^\infty \left(\boldsymbol{\tau}_n^* \boldsymbol{u}_m^* - \boldsymbol{\tau}_m^* \boldsymbol{u}_n^*\right)\mathrm{d}z \tag{A8}$$

Defining

$$P_{pq} = \int_0^\infty \left(\boldsymbol{\tau}_p \boldsymbol{u}_q - \boldsymbol{\tau}_q \boldsymbol{u}_p\right)\mathrm{d}z \tag{A9}$$

$$S_{pq} = \int_0^\infty \left(\boldsymbol{\tau}_p^* \boldsymbol{u}_q - \boldsymbol{\tau}_q \boldsymbol{u}_p^*\right)\mathrm{d}z \tag{A10}$$

then eqs (A7) and (A8) can be written as

$$a_m + \frac{1}{S_{mm}} \sum_{n=0}^{N} b_n P_{mn} = 0 \tag{A11}$$

$$\frac{1}{S_{nn}} \sum_{m=0}^{M} a_m P_{mn}^* + b_n = \frac{-1}{S_{nn}} S_{sn}^* \tag{A12}$$

Written in matrix form:

$$\begin{bmatrix} 1 & \cdots & 0 & \frac{P_{00}}{S_{00}^{(I)}} & \cdots & \frac{P_{0N}}{S_{00}^{(I)}} \\ \vdots & \ddots & \vdots & \vdots & \ddots & \vdots \\ 0 & \cdots & 1 & \frac{P_{M0}}{S_{MM}^{(I)}} & \cdots & \frac{P_{MN}}{S_{MM}^{(I)}} \\ \frac{P_{00}^*}{S_{00}^{(T)}} & \cdots & \frac{P_{M0}^*}{S_{00}^{(T)}} & 1 & \cdots & 0 \\ \vdots & \ddots & \vdots & \vdots & \ddots & \vdots \\ \frac{P_{0N}^*}{S_{NN}^{(T)}} & \cdots & \frac{P_{MN}^*}{S_{NN}^{(T)}} & 0 & \cdots & 1 \end{bmatrix} \begin{bmatrix} a_0 \\ \vdots \\ a_M \\ b_0 \\ \vdots \\ b_N \end{bmatrix} = \begin{bmatrix} 0 \\ \vdots \\ 0 \\ -\frac{S_{s0}^*}{S_{00}^{(T)}} \\ \vdots \\ -\frac{S_{sN}^*}{S_{NN}^{(T)}} \end{bmatrix} \tag{A13}$$

Reflection and transmission coefficients can be solved by matrix inversion.

P_{pq} and S_{pq} can be calculated by depth integration of displacement and stress eigenfunctions. The equations above works for both Rayleigh and Love waves although the eigenfunctions involved differ. Here we focus on Rayleigh waves. Following Aki & Richards (2002, p. 263), the displacement and stress eigenfunctions of a layered model can be represented as:

$$\begin{aligned} u_x &= r_1(k,z,\omega)\, e^{i(kx-\omega t)},\ u_y = 0,\ u_z = i r_2(k,z,\omega)\, e^{i(kx-\omega t)} \\ \tau_{zx} &= \mu\left(\frac{\partial r_1}{\partial z} - k r_2\right) e^{i(kx-\omega t)} = r_3(k,z,\omega)\, e^{i(kx-\omega t)} \\ \tau_{zz} &= i\left[(\lambda+2\mu)\frac{\partial r_2}{\partial z} + k\lambda r_1\right] e^{i(kx-\omega t)} = i r_4(k,z,\omega)\, e^{i(kx-\omega t)} \\ \tau_{xx} &= i\left[\lambda\frac{r_4 - k\lambda r_1}{\lambda+2\mu} + k(\lambda+2\mu) r_1\right] e^{i(kx-\omega t)} = i r_5 e^{i(kx-\omega t)} \end{aligned} \tag{A14}$$

Four independent eigenfunctions r_1, r_2, r_3 and r_4 can be solved by propagator matrix methods (Aki & Richards 2002; Denolle *et al.* 2012). We use code from Herrmann (2013) to calculate eigenfunctions, which are normalized by the vertical displacement at the surface ($z = 0$) for each mode. We correct the signs of the eigenfunction from Herrmann (2013; z-axis positive direction upward) to be consistent with the convention from Aki & Richards (2002; z-axis positive direction downward). The fifth eigenfunction r_5 can be calculated from eq. (A14) afterwards. We then have

$$\begin{aligned} P_{pq} &= \int_0^\infty \left(\boldsymbol{\tau}_p \boldsymbol{u}_q - \boldsymbol{\tau}_q \boldsymbol{u}_p\right)\mathrm{d}z \\ &= \int_0^\infty \left[\left(i r_5^p \hat{x} + r_3^p \hat{z}\right)\left(r_1^q \hat{x} + i r_2^q \hat{z}\right) - \left(i r_5^q \hat{x} + r_3^q \hat{z}\right)\left(r_1^p \hat{x} + i r_2^p \hat{z}\right)\right]\mathrm{d}z \\ &= i\int_0^\infty \left(r_5^p r_1^q + r_3^p r_2^q - r_5^q r_1^p - r_3^q r_2^p\right)\mathrm{d}z \end{aligned} \tag{A15}$$

$$\begin{aligned} S_{pq} &= \int_0^\infty \left(\boldsymbol{\tau}_p^* \boldsymbol{u}_q - \boldsymbol{\tau}_q \boldsymbol{u}_p^*\right)\mathrm{d}z \\ &= \int_0^\infty \left[\left(i r_5^p \hat{x} + r_3^p \hat{z}\right)^*\left(r_1^q \hat{x} + i r_2^q \hat{z}\right) - \left(i r_5^q \hat{x} + r_3^q \hat{z}\right)\left(r_1^p \hat{x} + i r_2^p \hat{z}\right)^*\right]\mathrm{d}z \\ &= i\int_0^\infty \left(-r_5^p r_1^q + r_3^p r_2^q - r_5^q r_1^p + r_3^q r_2^p\right)\mathrm{d}z \end{aligned} \tag{A16}$$

where superscripts of eigenfunctions p and q are mode indices of the medium they are in. This concludes the algorithm to calculate the Rayleigh reflection and transmission coefficients at a vertical boundary.